

Transport Effects on Multiple-Component Reactions in Optical Biosensors

Ryan M. Evans · David A. Edwards

Received: date / Accepted: date

Abstract Many biochemical reactions involve a stream of chemical reactants (ligand molecules) flowing over a surface to which other reactants (receptors) are confined. Scientists measure rate constants associated with these reactions in an optical biosensor: an instrument in which ligand molecules are convected through a flow cell, over a surface on which receptors are immobilized. In applications such as DNA damage repair multiple simultaneous reactions occur on the surface of the biosensor. We quantify transport effects on such multiple-component reactions, which result in a nonlinear set of integrodifferential equations for the reacting species concentrations. In physically relevant parameter regimes, these integrodifferential equations further reduce to a nonlinear set of ordinary differential equations, which may be used to estimate rate constants from biosensor data. We verify our results with a semi-implicit finite difference algorithm.

Keywords Biochemistry · Optical biosensors · Rate constants · Partial differential equations · Integrodifferential equations · Numerical methods

1 Introduction

Many biochemical reactions in nature involve a stream of chemical reactants (*ligand molecules*) flowing through a fluid-filled volume, and another reactant (*recep-*

This work was done with the support of the National Science Foundation under award number nsf-dms 1312529, and was also partially supported by the National Research Council through an NRC postdoctoral fellowship.

R. M. Evans
Applied and Computational Mathematics Division, Information and Technology Lab,
National Institute for Standards and Technology, Gaithersburg, MD 20899, USA
E-mail: ryan.evans@nist.gov

D. A. Edwards
Department of Mathematical Sciences, University of Delaware, Newark, DE 19716, USA
E-mail: dedwards@udel.edu

tors) confined to a surface. Such surface-volume reactions occur during platelet adhesion (Austin, 2009), drug absorption (Bertucci et al., 2007), antigen-antibody interactions (Raghaven et al., 1994), and DNA damage repair (Zhuang et al., 2008). Fundamental to understanding these reactions is getting accurate quantitative measurements of the underlying *reaction rate constants*. To measure rate constants associated with surface-volume reactions, scientists use *optical biosensors*: see Figure 1.1 for a schematic of one such instrument; here, $\tilde{x} = 0$ corresponds to the inlet and $\tilde{y} = 0$ corresponds to the sensor surface. Biosensor technology has become extremely popular in recent years; 10,000 papers have cited the use of an optical biosensor as of 2009 alone (Rich and Myszk, 2011).

For our purposes, biosensor experiments are partitioned into two phases: the injection phase, and the wash phase. During the injection phase, ligand molecules are injected into the biosensor via a buffer fluid in a standard two-dimensional Poiseuille flow profile from the inlet at $\tilde{x} = 0$ at concentration $\tilde{C}(\tilde{x}, \tilde{y}, \tilde{t})$; the tilde variables denote dimensional quantities throughout. The ligand molecules then diffuse through the buffer onto the channel floor to bind with receptors immobilized on the surface. Mass changes on the floor due to ligand binding are averaged over a portion of the channel floor $[\tilde{x}_{\min}, \tilde{x}_{\max}]$ to produce measurements of the form

$$\tilde{B}(t) = \frac{1}{\tilde{x}_{\max} - \tilde{x}_{\min}} \int_{\tilde{x}_{\min}}^{\tilde{x}_{\max}} \tilde{B}(\tilde{x}, \tilde{t}) d\tilde{x}, \quad (1.1)$$

where $\tilde{B}(\tilde{x}, \tilde{t})$ is the concentration of bound ligand molecules. After the bound state reaches a chemical equilibrium, scientists then prepare the device for another experiment by washing it with the buffer fluid—this is the wash phase of the experiment. Only buffer is flowing through the biosensor during the wash phase, not buffer containing the ligand molecules. This has the effect of causing all bound ligand molecules to get swept out of the biosensor, thereby cleaning the device for another experiment.

Measuring rate constants with biosensor data relies on having an accurate mathematical model of this process; mathematical models have been successfully proposed and progressively refined throughout the years: (Edwards, 1999, 2000, 2001, 2006, 2011; Edwards et al., 1999; Lebedev et al., 2006; Zumbrum and Edwards, 2014, 2015). Although such mathematical models are typically limited to reactions involving only a single molecule or a single step, chemists are currently using biosensor technology to measure rate constants associated with reactions involving multiple components. For example, chemists are now using biosensor experiments to elucidate how cells cope with DNA damage. Harmful DNA lesions can impair a cell's ability to replicate DNA, and its ability to survive. One way a cell may respond to a DNA lesion is through DNA translesion synthesis (Friedberg, 2005; Lehmann et al., 2007; Plosky and Woodgate, 2004). For a description of this process we refer the interested reader to the references included herein; however, for our purposes it is sufficient to know that DNA translesion synthesis involves multiple interacting components: a Proliferating Cell Nuclear Antigen (PCNA) molecule, polymerase δ , and polymerase η . Further, in order for a successful DNA translesion synthesis event to occur polymerase δ must bind with a PCNA molecule. A central question surrounding DNA translesion synthesis is whether polymerase δ directly binds with the

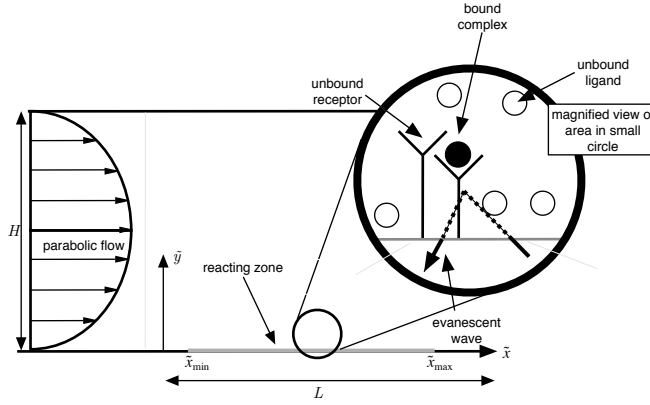


Fig. 1.1: Cross-sectional schematic of an optical biosensor experiment. The instrument has length \tilde{L} and height \tilde{H} . Ligand molecules are convected into instrument in a Poiseuille flow profile and transported to the surface to bind with receptors. The receptors are limited to the reacting zone $\tilde{x} = \tilde{x}_{\min}$ to $\tilde{x} = \tilde{x}_{\max}$.

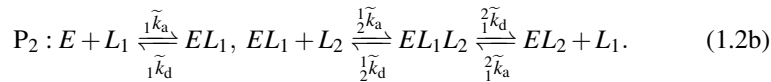
PCNA, or whether the polymerase δ and PCNA complex forms as a result of a *ligand switching process* (Zhuang et al., 2008).

The former scenario is depicted in Figure 1.2, where we have shown polymerase δ directly binding with a PCNA molecule, *i.e.* the reaction:



Here, we have denoted the PCNA molecule and polymerase δ as E and L_2 respectively. Additionally, $2\tilde{k}_a$ denotes the rate at which L_2 binds with a PCNA molecule E , and $2\tilde{k}_d$ denotes the rate at which L_2 dissociates from a PCNA molecule E . We will refer to this as pathway one, or simply P_1 as in (1.2a).

The ligand switching process is shown in Figure 1.3 and stated precisely as:



First, polymerase η (denoted L_1) binds with a PCNA molecule; next polymerase δ associates with the polymerase η and PCNA complex; finally polymerase η switches out, thereby leaving us with the polymerase δ and PCNA complex. Each one of the steps in this multiple-component process is reversible. In (1.2b) and Figure 1.3, the rate constants $1\tilde{k}_a$ and $1\tilde{k}_d$ denote the rates at which polymerase η binds and unbinds with a PCNA molecule (respectively), $i\tilde{k}_a$ denotes the rate at which ligand L_i binds with the product EL_j , and $i\tilde{k}_d$ denotes the rate at which L_i dissociates from the product EL_1L_2 . In the latter two expressions the indices i and j can equal one or two. We shall refer to this pathway two, or simply P_2 as in (1.2b).

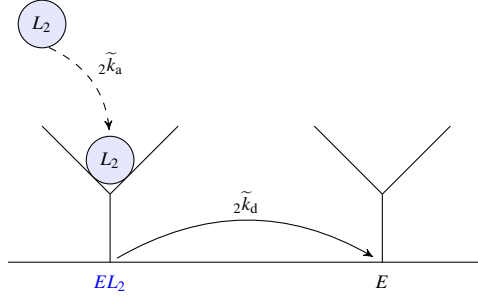


Fig. 1.2: Direct binding of polymerase δ with a PCNA molecule. We have labeled polymerase δ and the PCNA molecule as L_2 and E respectively.

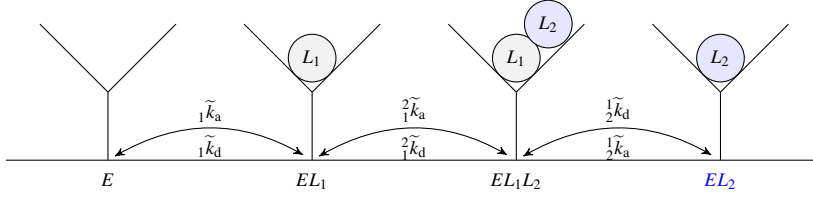


Fig. 1.3: Schematic of the ligand switching process. First, polymerase η binds with the PCNA molecule; next, polymerase δ binds with the polymerase η and PCNA complex; finally, polymerase η dissociates, leaving us with the polymerase δ and PCNA complex. We have labeled polymerase η , polymerase δ , and the PCNA molecule as L_1 , L_2 , and E respectively.

By measuring the rate constants associated with this multiple-component process, one could therefore determine whether EL_2 forms as a result of ligand binding or the ligand switching process described above. To measure the kinetic rate constants, scientists first immobilize PCNA molecules on the surface of the biosensor. After receptor immobilization, scientists inject L_1 and L_2 into the instrument at concentrations $\tilde{C}_1(\tilde{x}, \tilde{y}, \tilde{t})$ and $\tilde{C}_2(\tilde{x}, \tilde{y}, \tilde{t})$. The ligands L_1 and L_2 are then transported to the surface to bind with available receptor sites E , creating the three products EL_1 , EL_1L_2 , and EL_2 at concentrations $\tilde{B}_1(\tilde{x}, \tilde{t})$, $\tilde{B}_{12}(\tilde{x}, \tilde{t})$, and $\tilde{B}_2(\tilde{x}, \tilde{t})$.

The presence of multiple reacting species changes the form of biosensor feedback (*i.e.*, the sensogram reading). Most optical biosensors measure only mass changes at the surface due to ligand binding, and produce lumped measurements of the form

$$\tilde{\mathcal{S}}(\tilde{t}) = \tilde{s}_1 \tilde{B}_1(\tilde{t}) + (\tilde{s}_1 + \tilde{s}_2) \tilde{B}_{12}(\tilde{t}) + \tilde{s}_2 \tilde{B}_2(\tilde{t}), \quad (1.3)$$

where $\tilde{B}_i(\tilde{t})$ is defined analogously to (1.1). Measuring rate constants associated with this multiple-component process involves calculating the sensogram signal (1.3), which relies on a mathematical model. The straightforward well-stirred kinetics approximation is inappropriate since it does not account for mechanisms which transport ligand molecules to the reacting surface. Though transport effects on bimolecular

kinetics are well studied, few if any attempts have been made to analytically quantify such effects on multiple-component reactions. Hence, we model the full convection-diffusion system with multiple coupled reactions at the boundary. High Péclet number flow implies that transport effects are relevant only in a thin unstirred region near the surface, and our Partial Differential Equation (PDE) system reduces asymptotically to a coupled nonlinear set of Integrodifferential Equations (IDEs). In physically relevant parameter regimes, this set of IDEs further simplifies to a set of Ordinary Differential Equations (ODEs), which can be used to determine the rate constants from biosensor data. By comparing the solution of our ODE system with a semi-implicit finite-difference solution to the IDE system, we show that this reduction holds for a wide parameter range, thus providing experimentalists with a tool to measure the rate constants in (1.2) and reveal the underlying pathway of polymerase δ in DNA translesion synthesis.

We remark that the above discussion may raise uniqueness concerns, since more than one set of rate constants may possibly correspond to the same signal (1.3). Fortunately, through varying the uniform in-flow concentrations of the ligands, $C_1(0, \tilde{y}, \tilde{t}) = \tilde{C}_{1,u}$ and $\tilde{C}_2(0, \tilde{y}, \tilde{t}) = \tilde{C}_{2,u}$, one may resolve this ill-posedness in certain physically relevant scenarios (Evans, R. M. and Edwards, D. A. and Li, W., in preparation). This approach to identifying the correct set of rate constants in the presence of ambiguous data is related to the “global analysis” technique in biological literature (Karlsson and Fält, 1997; Morton et al., 1995).

2 Governing Equations

2.1 Injection Phase

We now present the equations governing reaction kinetics during the injection phase; to this end we let

$$\tilde{\mathbf{B}}(\tilde{x}, \tilde{t}) = (\tilde{B}_1(\tilde{x}, \tilde{t}), \tilde{B}_{12}(\tilde{x}, \tilde{t}), \tilde{B}_2(\tilde{x}, \tilde{t}))^T$$

denote a vector in \mathbb{R}^3 whose components are the three bound state concentrations; $\tilde{B}_\Sigma = \tilde{B}_1 + \tilde{B}_{12} + \tilde{B}_2$; and \tilde{R}_T denote the initial empty receptor concentration. Note, the total concentration of empty receptors at any point during the experiment is given by $[E](\tilde{x}, \tilde{t}) = \tilde{R}_T - \tilde{B}_\Sigma(\tilde{x}, \tilde{t})$. Applying the law of mass action to (1.2a) and (1.2b) gives the following set of partial differential equations for $\tilde{B}_i(\tilde{x}, \tilde{t})$:

$$\begin{aligned} \frac{\partial \tilde{B}_1}{\partial \tilde{t}} &= {}_1\tilde{k}_a(\tilde{R}_T - \tilde{B}_\Sigma)\tilde{C}_1(\tilde{x}, 0, \tilde{t}) + {}_2\tilde{k}_d\tilde{B}_{12} - {}_1\tilde{k}_d\tilde{B}_1 - {}_2\tilde{k}_a\tilde{B}_1\tilde{C}_2(\tilde{x}, 0, \tilde{t}), \\ \frac{\partial \tilde{B}_{12}}{\partial \tilde{t}} &= {}_1\tilde{k}_a\tilde{B}_1\tilde{C}_2(\tilde{x}, 0, \tilde{t}) + {}_2\tilde{k}_a\tilde{B}_2\tilde{C}_1(\tilde{x}, 0, \tilde{t}) - {}_1\tilde{k}_d\tilde{B}_{12} - {}_2\tilde{k}_d\tilde{B}_{12}, \\ \frac{\partial \tilde{B}_2}{\partial \tilde{t}} &= {}_2\tilde{k}_a(\tilde{R}_T - \tilde{B}_\Sigma)\tilde{C}_2(\tilde{x}, 0, \tilde{t}) + {}_1\tilde{k}_d\tilde{B}_{12} - {}_2\tilde{k}_d\tilde{B}_2 - {}_1\tilde{k}_a\tilde{B}_2\tilde{C}_1(\tilde{x}, 0, \tilde{t}), \\ \tilde{\mathbf{B}}(\tilde{x}, 0) &= \mathbf{0}; \end{aligned} \tag{2.1}$$

these equations hold on the reacting surface when $\tilde{y} = 0$ and $\tilde{x} \in [0, \tilde{L}]$. The instrument's height \tilde{H} is much less than its length \tilde{L} , hence its aspect ratio $\varepsilon = \tilde{H}/\tilde{L}$ is small.

On the reacting surface at $\tilde{y} = 0$, the diffusive flux of ligand is used up in binding to form the various bound states:

$$\begin{aligned} -\tilde{D}_1 \frac{\partial \tilde{C}_1}{\partial \tilde{y}}(\tilde{x}, 0, \tilde{t}) = & -{}_1\tilde{k}_a(\tilde{R}_T - \tilde{B}_\Sigma)\tilde{C}_1(\tilde{x}, 0, \tilde{t}) + {}_1\tilde{k}_d\tilde{B}_1 \\ & - {}_1^2\tilde{k}_a\tilde{B}_2\tilde{C}_1(\tilde{x}, 0, \tilde{t}) + {}_1^2\tilde{k}_d\tilde{B}_{12}, \end{aligned} \quad (2.2a)$$

$$\begin{aligned} -\tilde{D}_2 \frac{\partial \tilde{C}_2}{\partial \tilde{y}}(\tilde{x}, 0, \tilde{t}) = & -{}_2\tilde{k}_a(\tilde{R}_T - \tilde{B}_\Sigma)\tilde{C}_2(\tilde{x}, 0, \tilde{t}) + {}_2\tilde{k}_d\tilde{B}_2 \\ & - {}_2^1\tilde{k}_a\tilde{B}_1\tilde{C}_2(\tilde{x}, 0, \tilde{t}) + {}_2^1\tilde{k}_d\tilde{B}_{12}. \end{aligned} \quad (2.2b)$$

Here \tilde{D}_1 and \tilde{D}_2 (respectively) denote the diffusion rates of L_1 and L_2 through the buffer. The four terms on the right-hand side of (2.2a) are (in order): loss of \tilde{C}_1 to an empty receptor to form \tilde{B}_1 ; dissociation of \tilde{B}_1 , which adds to \tilde{C}_1 ; loss of \tilde{C}_1 to \tilde{B}_2 to form \tilde{B}_{12} ; and dissociation of \tilde{B}_{12} into \tilde{B}_2 and \tilde{C}_1 . The terms on the right-hand side of (2.2b) have similar interpretations. But then using (2.1), we have

$$\tilde{D}_1 \frac{\partial \tilde{C}_1}{\partial \tilde{y}}(\tilde{x}, 0, \tilde{t}) = \frac{\partial \tilde{B}_1(\tilde{x}, \tilde{t})}{\partial \tilde{t}} + \frac{\partial \tilde{B}_{12}(\tilde{x}, \tilde{t})}{\partial \tilde{t}}, \quad (2.3a)$$

$$\tilde{D}_2 \frac{\partial \tilde{C}_2}{\partial \tilde{y}}(\tilde{x}, 0, \tilde{t}) = \frac{\partial \tilde{B}_{12}(\tilde{x}, \tilde{t})}{\partial \tilde{t}} + \frac{\partial \tilde{B}_2(\tilde{x}, \tilde{t})}{\partial \tilde{t}}. \quad (2.3b)$$

We now present the evolution equations for the unbound concentrations $\tilde{C}_1(\tilde{x}, \tilde{y}, \tilde{t})$ and $\tilde{C}_2(\tilde{x}, \tilde{y}, \tilde{t})$. Due to the geometry of the device, a unidirectional flow model is appropriate (Zumbrum and Edwards, 2014). This Poiseuille channel flow leads to a parabolic velocity flow profile; thus, the convection-diffusion equations for $\tilde{C}_i(\tilde{x}, \tilde{y}, \tilde{t})$ take the form:

$$\frac{\partial \tilde{C}_i}{\partial \tilde{t}} = \tilde{D}_i \tilde{\nabla}^2 \tilde{C}_i - \tilde{\mathbf{v}} \cdot \tilde{\nabla} \tilde{C}_i, \quad \tilde{\mathbf{v}} = \left(\frac{\tilde{V}\tilde{y}}{\tilde{H}} \left(1 - \frac{\tilde{y}}{\tilde{H}} \right), 0 \right), \quad (2.4)$$

where $i = 1, 2$; the above equations hold when $(\tilde{x}, \tilde{y}) \in (0, \tilde{L}) \times (0, \tilde{H})$ and $\tilde{t} > 0$; and \tilde{V} is the characteristic velocity associated with our flow. Furthermore: initially there is no unbound ligand in the channel, ligand is convected in at uniform rates $\tilde{C}_{i,u}$ after the initial time $\tilde{t} = 0$, and no-flux conditions hold downstream at $\tilde{x} = \tilde{L}$ and on the ceiling at $\tilde{y} = \tilde{H}$.

Due to high Péclet number flow, Edwards has demonstrated (Edwards, 1999) that transport effects are relevant only in a thin unstirred layer near the surface, and that the appropriate dimensionless variables are:

$$\begin{aligned} x = \frac{\tilde{x}}{\tilde{L}}, \quad y = \frac{\tilde{y}}{\tilde{L}}, \quad \eta = \text{Pe}^{1/3} y, \quad \text{Pe} = \frac{\tilde{V}\tilde{H}^2}{\tilde{L}\tilde{D}_2}, \quad t = {}_1\tilde{k}_a\tilde{C}_{1,u}\tilde{t}, \\ B_i(x, t) = \frac{\tilde{B}_i(\tilde{x}, \tilde{t})}{\tilde{R}_T}, \quad C_i(x, \eta, t) = \frac{\tilde{C}_i(\tilde{x}, \tilde{y}, \tilde{t})}{\tilde{C}_{i,u}}. \end{aligned} \quad (2.5)$$

These are the natural scalings associated with the *reaction-limited* and *transport-dominant* parameter regime, in which ligand molecules are transported to the unstirred layer and gradually bind with receptor sites at the surface. Introducing the scalings (2.5) into (2.1) results in the dimensionless bound state system:

$$\frac{\partial B_1}{\partial t} = (1 - B_\Sigma)C_1 + {}_2K_d B_{12} - {}_1K_d B_1 - {}_2K_a B_1 C_2, \quad (2.6a)$$

$$\frac{\partial B_{12}}{\partial t} = {}_2K_a B_1 C_2 + {}_1K_a B_2 C_1 - {}_2K_d B_{12} - {}_1K_d B_{12}, \quad (2.6b)$$

$$\frac{\partial B_2}{\partial t} = {}_2K_a (1 - B_\Sigma)C_2 + {}_1K_d B_{12} - {}_2K_d B_2 - {}_1K_a B_2 C_1. \quad (2.6c)$$

$$\mathbf{B}(x, 0) = \mathbf{0}, \quad (2.6d)$$

on the surface at $\eta = 0$. The dimensionless rate constants in (2.6) are defined as:

$${}_i^j K_a = \frac{\tilde{C}_{i,u} \cdot {}_i^j \tilde{k}_a}{\tilde{C}_{1,u} \cdot {}_1 \tilde{k}_a}, \quad {}_i^j K_d = \frac{\tilde{k}_d}{\tilde{C}_{1,u} \cdot {}_1 \tilde{k}_a},$$

where $i = 1, 2$, and $j = 1, 2$, or can be blank (${}_i K_a$ and ${}_i K_d$ are the dimensionless analogs of ${}_i k_a$, or ${}_i k_d$). We non-dimensionalize the sensogram reading (1.3) by setting

$$\mathcal{S}(t) = \frac{\tilde{\mathcal{S}}(t)}{\tilde{R}_T \cdot \tilde{s}_1} = \bar{B}_1(t) + \left(1 + \frac{\tilde{s}_2}{\tilde{s}_1}\right) \bar{B}_{12}(t) + \frac{\tilde{s}_2}{\tilde{s}_1} \bar{B}_2(t). \quad (2.7)$$

The diffusive flux conditions (2.3) become:

$$\frac{\partial C_1}{\partial \eta}(x, 0, t) = \frac{\text{Da}}{F_r} \left(\frac{\partial B_1}{\partial t} + \frac{\partial B_{12}}{\partial t} \right), \quad (2.8a)$$

$$\frac{\partial C_2}{\partial \eta}(x, 0, t) = \text{Da} \left(\frac{\partial B_{12}}{\partial t} + \frac{\partial B_2}{\partial t} \right), \quad (2.8b)$$

where

$$\text{Da} = \frac{{}_1 \tilde{k}_a \tilde{R}_T (\tilde{H}\tilde{L})^{1/3}}{(\tilde{V}\tilde{D}^2)^{1/3}}, \quad F_r = C_r D_r, \quad C_r = \frac{\tilde{C}_{1,u}}{\tilde{C}_{2,u}}, \quad D_r = \frac{\tilde{D}_1}{\tilde{D}_2}. \quad (2.9)$$

The Damköhler number, denoted Da , is a key dimensionless group which represents the relative strength of reaction to diffusion. In practice, it is desirable to design biosensor experiments such that $\text{Da} \ll 1$. When $\text{Da} \ll 1$, diffusion and reaction occur on different time scales, and one is in the best position to measure reaction. Typically this is the case, although at times experimentalists can only increase velocities enough to make $\text{Da} = O(1)$ (Edwards, 1999). Further, F_r measures the diffusion strength of each reacting species, as characterized by the product of the input concentrations and the diffusion coefficients.

It remains to derive the equations for the unbound concentrations $C_i(x, \eta, t)$ in the unstirred layer. To this end, we substitute the dimensionless variables (2.5) into

(2.4) and expand the result in a perturbation series for large Pe . The leading order equations are:

$$D_r \frac{\partial^2 C_1}{\partial \eta^2} = \eta \frac{\partial C_1}{\partial x}, \quad (2.10a)$$

$$\frac{\partial^2 C_2}{\partial \eta^2} = \eta \frac{\partial C_2}{\partial x}, \quad (2.10b)$$

with the boundary data:

$$C_i(0, \eta, t) = 1, \quad (2.11a)$$

$$\lim_{\eta \rightarrow \infty} C_i(x, \eta, t) = 1, \quad (2.11b)$$

and equations (2.8). Equation (2.11a) tells us that at $x = 0$, the concentration is given by the normalized inlet value. Equation (2.11b) expresses the requirement that as one exits the unstirred layer, *i.e.* as $\eta \rightarrow \infty$, the concentration must match the undisturbed value in the bulk flow. A more detailed description of this process may be found in (Edwards, 1999).

To study (2.6) we need the value of C_i only on the reacting surface at $\eta = 0$. By analogy with (Edwards, 1999) we can transform (2.10a) and (2.10b) into Airy's equations through a Laplace transform in x . The derivative of the transformed solution at $\eta = 0$ is known, so one can show

$$C_1(x, 0, t) = 1 - \frac{D_r^{1/3} Da}{F_r \Gamma(2/3) 3^{1/3}} \int_0^x \left(\frac{\partial B_1}{\partial t} + \frac{\partial B_{12}}{\partial t} \right) (v, t) \frac{dv}{(x-v)^{2/3}}, \quad (2.12a)$$

$$C_2(x, 0, t) = 1 - \frac{Da}{\Gamma(2/3) 3^{1/3}} \int_0^x \left(\frac{\partial B_{12}}{\partial t} + \frac{\partial B_2}{\partial t} \right) (v, t) \frac{dv}{(x-v)^{2/3}}. \quad (2.12b)$$

Early in the experiment, ligand molecules diffuse to the surface to bind with receptor sites upstream, before they do so downstream. This phenomenon of upstream ligand depletion is reflected in (2.12), and readily seen in Figure 2.1; here we have depicted results of our numerical method described in Section 4. Thus, during the injection phase the bound state evolution is governed by the IDE system (2.6), with (2.12).

2.2 Wash Phase

We now present the relevant dimensionless equations for the wash phase. In practice, the injection phase is run until the bound state concentration reaches a steady state (Rich and Myszk, 2009). Since the bound ligand concentration evolves on a much slower time scale than the unbound ligand concentration (Edwards, 1999), the unbound ligand will have also reached steady state by the time the wash phase begins; *i.e.*, $C_i(x, y, 0) = 1$ for $(x, y) \in [0, 1]^2$, at the start of the wash phase. The reaction kinetics are therefore governed by (2.6), with (2.6d) replaced by the steady state solution

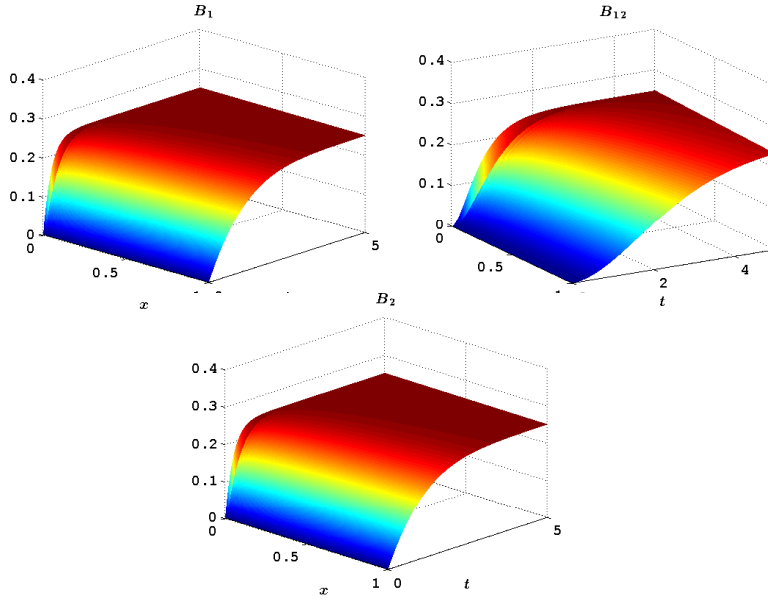


Fig. 2.1: Injection phase of biosensor experiment, up to $t = 5$, obtained through solving (2.6), (2.12) with the numerical method described in Section 4. All rate constants were taken equal to one, and Da taken equal to two to visualize upstream ligand depletion, which is especially evident in B_{12} .

to (2.6) during the injection phase:

$$\mathbf{B}(x, 0) = A^{-1} \mathbf{f}, \quad (2.13)$$

$$A = \begin{pmatrix} (1 + {}_1K_d + {}_2K_a) & 1 - {}_1K_d & 1 \\ -{}_2K_a & ({}_2K_d + {}_1K_d) & -{}_1K_a \\ {}_2K_a & {}_2K_a - {}_1K_d & ({}_2K_a + {}_2K_d + {}_1K_a) \end{pmatrix}, \quad (2.14)$$

$$\mathbf{f} = \begin{pmatrix} 1 \\ 0 \\ {}_2K_a \end{pmatrix}. \quad (2.15)$$

Equations similar to (2.11b) hold:

$$C_i(0, \eta, t) = 0, \quad (2.16a)$$

$$\lim_{\eta \rightarrow \infty} C_i(x, \eta, t) = 0. \quad (2.16b)$$

Equation (2.16a) is the inflow condition, and (2.16b) expresses the requirement that the concentration in the layer must match the concentration $C_i(x, y, t) = 0$ in the outer layer. In a similar manner to the injection phase, one can use (2.10) together with (2.16) to show

$$C_1(x, 0, t) = -\frac{D_r^{1/3} \text{Da}}{F_r \Gamma(2/3) 3^{1/3}} \int_0^x \left(\frac{\partial B_1}{\partial t} + \frac{\partial B_{12}}{\partial t} \right) (v, t) \frac{dv}{(x-v)^{2/3}}, \quad (2.17a)$$

$$C_2(x, 0, t) = -\frac{\text{Da}}{\Gamma(2/3) 3^{1/3}} \int_0^x \left(\frac{\partial B_{12}}{\partial t} + \frac{\partial B_2}{\partial t} \right) (v, t) \frac{dv}{(x-v)^{2/3}}. \quad (2.17b)$$

Thus, during the wash phase, the bound state evolution is governed by the IDE system (2.6a)–(2.6c), (2.13), and (2.17).

3 Effective Rate Constant Approximation

During both phases of the experiment, the bound state concentration obeys a nonlinear set of IDEs which is hopeless to solve in closed form. Moreover, we are ultimately interested in the average concentration $\bar{\mathbf{B}}(t)$ —not $\mathbf{B}(x, t)$ —since from $\bar{\mathbf{B}}(t)$ we can reconstruct the sensogram signal (2.7) (*i.e.*, the quantity of physical relevance). Thus, we seek to find an approximation to $\bar{\mathbf{B}}(t)$, and begin by finding one during the injection phase. We first average each side of (2.6) and (2.12) in the sense of (1.1). Immediately, we are confronted with terms such as

$$\overline{B_1 C_2} = B_1 \left(1 - \frac{\text{Da}}{3^{1/3} \Gamma(2/3)} \int_0^x \left(\frac{\partial B_{12}}{\partial t} + \frac{\partial B_2}{\partial t} \right) \frac{dv}{(x-v)^{2/3}} \right), \quad (3.1)$$

on the right hand side of (2.6a). In the experimentally relevant case of small Da, we are motivated to expand $\mathbf{B}(x, t)$ in a perturbation series:

$$\mathbf{B}(x, t) = {}^0\mathbf{B}(x, t) + O(\text{Da}). \quad (3.2)$$

In this limit, the leading order of (2.12) is just $C_i = 1$. Using this result in (2.6), we have that the governing equation for ${}^0\mathbf{B}$ is independent of x :

$$\frac{d {}^0\mathbf{B}}{dt} = -A {}^0\mathbf{B} + \mathbf{f},$$

where A is given by (2.14) and \mathbf{f} by (2.15). Hence the leading-order approximation

$${}^0\mathbf{B}(t) = A^{-1} (I - e^{-At}) \mathbf{f} \quad (3.3)$$

is independent of space. Substituting (3.3) into (2.12), the time-dependent terms may be factored out of the integrand, leaving the spatial dependence of C_j varying as $x^{1/3}$. This is the only spatial variation in (2.6) at $O(\text{Da})$; hence we may write

$$\mathbf{B}(x, t) = {}^0\mathbf{B}(t) + \text{Da } x^{1/3} \cdot {}^1\mathbf{B}(t) + O(\text{Da}^2). \quad (3.4)$$

As a result of (3.4) we have the relation

$$\text{Da } B_i(x, t) = \text{Da } {}^0B_i(t) + O(\text{Da}^2), \quad (3.5)$$

which may be used to show the right hand side of (3.1) is equal to

$$\bar{B}_1 - \text{Da} \bar{h} \cdot {}^0B_1 \left(\frac{d^0B_{12}}{dt} + \frac{d^0B_2}{dt} \right) + O(\text{Da}^2), \quad (3.6)$$

$$h(x) = \frac{3^{2/3} x^{1/3}}{\Gamma(2/3)}.$$

Then, by applying (3.5) to (3.6) equation (3.1) reduces to

$$\overline{B_1 C_2} = \bar{B}_1 \left[1 - \text{Da} \bar{h} \left(\frac{d\bar{B}_{12}}{dt} + \frac{d\bar{B}_2}{dt} \right) \right] + O(\text{Da}^2).$$

In this manner, we can derive a set of nonlinear ODEs for $\bar{\mathbf{B}}(t)$ of the form:

$$\frac{d\bar{\mathbf{B}}}{dt} = M^{-1}(\bar{\mathbf{B}})(-A\bar{\mathbf{B}} + \mathbf{f}) + O(\text{Da}^2), \quad (3.7a)$$

$$\bar{\mathbf{B}}(0) = \mathbf{0}, \quad (3.7b)$$

where

$$M(\bar{\mathbf{B}}) = I + \text{Da} N(\bar{\mathbf{B}}),$$

$$N(\bar{\mathbf{B}}) = \begin{pmatrix} \frac{D_r^{1/3}\bar{h}}{F_r}(1 - \bar{B}_\Sigma) & \frac{D_r^{1/3}\bar{h}}{F_r}(1 - \bar{B}_\Sigma) - \frac{1}{2}K_a\bar{h} \cdot \bar{B}_1 & -\frac{1}{2}K_a\bar{h} \cdot \bar{B}_1 \\ \frac{1}{2}K_a\bar{h} \cdot \bar{B}_1 & \frac{1}{2}K_a\bar{h} \cdot \bar{B}_1 + \frac{1}{2}K_a\left(\frac{D_r^{1/3}\bar{h}}{F_r}\right)\bar{B}_2 & \frac{1}{2}K_a\left(\frac{D_r^{1/3}\bar{h}}{F_r}\right)\bar{B}_2 \\ -\frac{1}{2}K_a\left(\frac{D_r^{1/3}\bar{h}}{F_r}\right)\bar{B}_2 & -\frac{1}{2}K_a\left(\frac{D_r^{1/3}\bar{h}}{F_r}\right)\bar{B}_2 + \frac{1}{2}K_a\bar{h}(1 - \bar{B}_\Sigma) & \frac{1}{2}K_a\bar{h}(1 - \bar{B}_\Sigma) \end{pmatrix}.$$

Following (Edwards and Jackson, 2002), we refer to (3.7) as a set of *Effective Rate Constant (ERC) Equations*. These equations are simple, and far easier to solve numerically than (2.6), using (2.12). The ODE system (3.7) is readily solved using a standard iterative method, such as an adaptive fourth-order Runge-Kutta. Moreover, our ERC equations provide a convenient tool for estimating rate constants from raw data. We have also derived a set of ERC equations for the wash phase, which take the form:

$$\frac{d\bar{\mathbf{B}}}{dt} = M^{-1}(\bar{\mathbf{B}})(-\mathcal{D}\bar{\mathbf{B}}) + O(\text{Da}^2), \quad (3.8a)$$

$$\bar{\mathbf{B}}(0) = A^{-1}\mathbf{f}, \quad (3.8b)$$

$$\mathcal{D} = \begin{pmatrix} {}_1K_d & -\frac{1}{2}K_d & 0 \\ 0 & ({}_2K_d + \frac{1}{2}K_d) & 0 \\ 0 & -\frac{1}{2}K_d & {}_2K_d \end{pmatrix}; \quad (3.8c)$$

the matrix $M(\bar{\mathbf{B}})$ is as in the injection phase.

The solution of our ERC equations is depicted in Figure 3.1; the injection phase was run from $t = 0$ to $t = 5$, and the wash phase was run from $t = 5$ to $t = 10$. The corresponding sensogram reading is depicted in Figure 3.2. We took $\text{Da} = 0.1$ and all of the rate constants equal to one during each of the phases.

During the injection phase, we see that \bar{B}_1 and \bar{B}_2 reach equilibrium after approximately one second, while \bar{B}_{12} takes approximately two seconds. This is not a

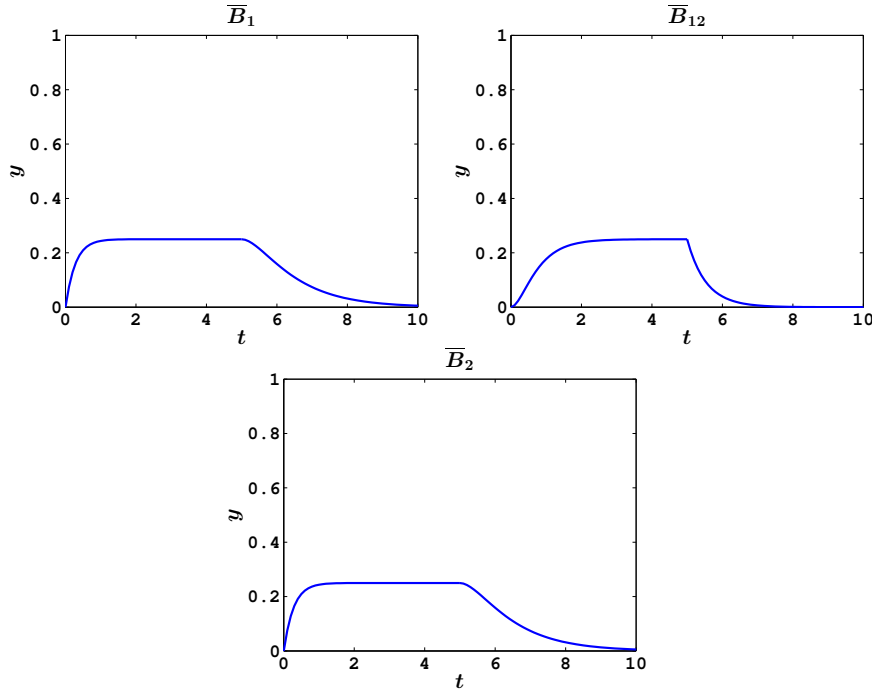


Fig. 3.1: The solution to our ERC equations. The first five seconds correspond to the solution of (3.7), while the last five seconds correspond to the solution of (3.8).

surprise: we are injecting equal amounts of both ligands, all the rate constants are the same, and either EL_1 or EL_2 must already be present in order for EL_1L_2 to form. Another consequence of these facts is that the chemical equilibria are equal; *i.e.*, the same balance between association and dissociation is achieved in each of the reacting species. Yet another result of these facts is that \bar{B}_{12} decays to zero before either of the other two reacting species; the reaction rates are the same, and the complex EL_1L_2 cannot transition directly into an empty receptor E .

4 Numerics

4.1 Semi-implicit finite difference algorithm

We now develop a semi-implicit finite difference algorithm to verify the accuracy of our ERC approximation; our finite difference method is based on the numerical method described in (Edwards and Jackson, 2002). Semi-implicit methods have been previously used with great success to solve reaction-diffusion equations (Nie et al., 2006), as they are typically robust, efficient, and accurate. Similarly, in our problem we exploit the structure of the integrodifferential operator (2.6), using (2.12), which naturally suggests a semi-implicit method in time.

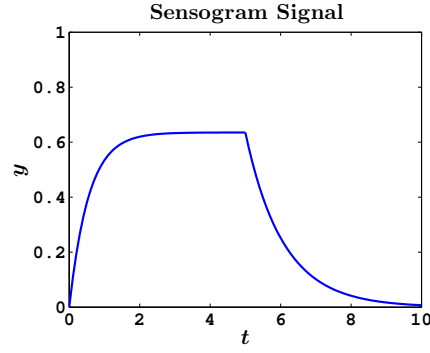


Fig. 3.2: The corresponding sensogram signal (2.7) to the reacting species in Figure 3.1.

We index space by i and time by n to write $B_{i,n}^j = B_j(i\Delta x, n\Delta t)$; doing so, our numerical method takes the form:

$$\begin{aligned}\frac{\partial B_{i,n+1}^1}{\partial t} &= (1 - B_{i,n}^\Sigma)C_{i,n+1}^1 + {}_2^1K_d B_{i,n}^{12} - {}_1K_d B_{i,n}^1 - {}_2^1K_a B_{i,n}^1 C_{i,n+1}^2, \\ \frac{\partial B_{i,n+1}^{12}}{\partial t} &= {}_2^1K_a B_{i,n}^1 C_{i,n+1}^2 + {}_1^2K_a B_{i,n}^2 C_{i,n+1}^1 - {}_2^1K_d B_{i,n}^{12} - {}_1^2K_d B_{i,n}^{12}, \\ \frac{\partial B_{i,n+1}^2}{\partial t} &= {}_2K_a (1 - B_{i,n}^\Sigma)C_{i,n+1}^2 + {}_1^2K_d B_{i,n}^{12} - {}_2K_d B_{i,n}^2 - {}_1^2K_a B_{i,n}^2 C_{i,n+1}^1,\end{aligned}$$

where

$$C_{i,n+1}^1 = 1 - \frac{D_r^{1/3} \text{Da}}{F_r 3^{1/3} \Gamma(\frac{2}{3})} \int_0^{x_i} \left(\frac{\partial B_1}{\partial t} + \frac{\partial B_{12}}{\partial t} \right) (x - v, t_{n+1}) \frac{dv}{v^{2/3}}, \quad (4.1a)$$

$$C_{i,n+1}^2 = 1 - \frac{\text{Da}}{3^{1/3} \Gamma(\frac{2}{3})} \int_0^{x_i} \left(\frac{\partial B_{12}}{\partial t} + \frac{\partial B_2}{\partial t} \right) (x_i - v, t_{n+1}) \frac{dv}{v^{2/3}}, \quad (4.1b)$$

during the injection phase. The convolution integrals $C_{i,n+1}^j$ have an analogous form during the wash phase. We impose the initial condition (either (2.6d) or (2.13)) at each of our $N + 1$ equally spaced discretization nodes x_i , for $i = 0, \dots, N$. We seek to discretize the convolution integrals using the trapezoidal rule; however (4.1a) and (4.1b) both have singular integrands. We subtract out the singularity at $v = 0$ by

writing (4.1a) and (4.1b) as:

$$C_{i,n+1}^1 = 1 - \frac{D_r^{1/3} \text{Da}}{F_r 3^{1/3} \Gamma(\frac{2}{3})} \left[\int_0^{x_i} \left\{ \left(\frac{\partial B_1}{\partial t} + \frac{\partial B_{12}}{\partial t} \right) (x_i - v, t_{n+1}) - \left(\frac{\partial B_{i,n+1}^1}{\partial t} + \frac{\partial B_{i,n+1}^{12}}{\partial t} \right) \right\} \frac{dv}{v^{2/3}} + 3x_i^{1/3} \left(\frac{\partial B_{i,n+1}^1}{\partial t} + \frac{\partial B_{i,n+1}^{12}}{\partial t} \right) \right] \quad (4.2a)$$

$$C_{i,n+1}^2 = 1 - \frac{\text{Da}}{3^{1/3} \Gamma(\frac{2}{3})} \left[\int_0^{x_i} \left\{ \left(\frac{\partial B_{12}}{\partial t} - \frac{\partial B_2}{\partial t} \right) (x_i - v, t_{n+1}) - \left(\frac{\partial B_{i,n+1}^{12}}{\partial t} + \frac{\partial B_{i,n+1}^2}{\partial t} \right) \right\} \frac{dv}{v^{2/3}} + 3x_i^{1/3} \left(\frac{\partial B_{i,n+1}^{12}}{\partial t} + \frac{\partial B_{i,n+1}^2}{\partial t} \right) \right]. \quad (4.2b)$$

We then proceed to discretize the convolution integrals with the trapezoidal rule, and time derivatives with a standard backwards difference formula. We march forward in time using a second-order Adams-Bashforth method. Additionally, since the convolution integral depends on x_j only for $j \leq i$, we compute values upstream first and march our way downstream at each time step. After computing our approximation $B_{i,n}^j$ at all of the desired time-steps, we may obtain an approximation to \bar{B}_j by averaging $B_{i,n}^j$ (in the sense of (1.1)) with the trapezoidal rule at each time step.

4.2 Convergence study

We now examine the convergence rate of our numerical method. We are achieving the expected $O(\Delta t^2)$ in time, thanks to our second-order Adams-Bashforth, so our analysis will focus on the rate of spatial convergence. We limit our analysis to the injection phase, and to the presence of a single reacting species on the sensor surface. Numerical evidence in Figure 4.1 and Table 4.1 suggests our analysis generalizes to our multiple-ligand model. In the bimolecular case, the relevant kinetics equation is given by (Edwards, 1999):

$$\frac{\partial B}{\partial t} = (1 - B)C(x, 0, t) - KB, \quad (4.3a)$$

$$C(x, 0, t) = 1 - \frac{\text{Da}}{3^{1/3} \Gamma(2/3)} \int_0^x \frac{\partial B}{\partial t}(v, t) \frac{dv}{(x - v)^{2/3}}, \quad (4.3b)$$

$$K = \frac{\tilde{k}_d}{\tilde{C}_u \tilde{k}_a}, \quad (4.3c)$$

where \tilde{C}_u is the inflow concentration, and \tilde{k}_a and \tilde{k}_d are the bimolecular association and dissociation rate constants. Moreover, one may show an approximation to the solution of (4.3) has the form (Edwards, 1999):

$$B(x, t) = {}^0B(t) + \text{Da } x^{1/3} \cdot {}^1B(t) + O(\text{Da}^2), \quad (4.4a)$$

$${}^0B(t) = \alpha^{-1}(1 - e^{-\alpha t}), \quad (4.4b)$$

$$\alpha = 1 + K, \quad (4.4c)$$

when $\text{Da} \ll 1$. The heart of our analysis lies in the $x^{1/3}$ spatial-dependence in (4.4a). Although the time-dependent functions ${}^0\mathbf{B}(t)$, ${}^1\mathbf{B}(t)$ in (3.4) are more complicated than ${}^0B(t)$, ${}^1B(t)$, the $x^{1/3}$ spatial-dependence is the same. Since (4.3) is nonlinear, we rely on (4.4a) when deriving spatial convergence estimates, and limit ourselves to the physically realistic case of $\text{Da} \ll 1$.

To determine the spatial rate of convergence of \bar{B} , we consider the averaged variant of (4.3), given by:

$$\begin{aligned} \frac{d\bar{B}}{dt} = & \overline{(1-B) \left(1 - \frac{\text{Da}}{3^{1/3}\Gamma(2/3)} \int_0^x \left(\frac{\partial B}{\partial t}(x-v, t) - \frac{\partial B}{\partial t}(x, t) \right) v^{-2/3} dv \right)} \\ & + \frac{\text{Da}(1-B)}{3^{1/3}\Gamma(2/3)} \cdot \overline{\left(3x^{1/3} \frac{\partial B}{\partial t}(x, t) \right)} - K\bar{B}, \end{aligned} \quad (4.5a)$$

$$\bar{B}(0) = 0. \quad (4.5b)$$

Notice we have subtracted out the singularity in the integrand of the convolution integral, at $v = 0$. We incur spatial error from each of the terms:

$$\overline{KB}, \quad (4.6a)$$

$$\frac{\text{Da}}{3^{1/3}\Gamma(2/3)} \overline{x^{1/3} \frac{\partial B}{\partial t}}, \quad (4.6b)$$

$$\frac{\text{Da}}{3^{1/3}\Gamma(2/3)} \overline{x^{1/3} B \frac{\partial B}{\partial t}}, \quad (4.6c)$$

$$\frac{\text{Da}}{3^{1/3}\Gamma(2/3)} \overline{\int_0^x \left(\frac{\partial B}{\partial t}(x-v, t) - \frac{\partial B}{\partial t}(x, t) \right) v^{-2/3} dv}, \quad (4.6d)$$

$$\frac{\text{Da}B}{3^{1/3}\Gamma(2/3)} \overline{\int_0^x \left(\frac{\partial B}{\partial t}(x-v, t) - \frac{\partial B}{\partial t}(x, t) \right) v^{-2/3} dv}. \quad (4.6e)$$

Let us denote the trapezoidal rule by $\mathcal{T}(\cdot, [a, b])$. By using (4.4a) and the fact that $\mathcal{T}(x^{1/3}, [x_{\min}, x_{\max}])$ converges at a rate of $O(\Delta x^2)$, one can show the terms (4.6a)–(4.6c) each converge at a rate of $O(\text{Da} \Delta x^2)$.

Now consider the term (4.6d); by definition, (4.6d) is written as

$$\frac{\text{Da}}{3^{1/3}\Gamma(2/3)(x_{\max} - x_{\min})} \int_{x_{\min}}^{x_{\max}} \int_0^x \left(\frac{\partial B}{\partial t}(x-v, t) - \frac{\partial B}{\partial t}(x, t) \right) v^{-2/3} dv dx.$$

Using (4.4a), the above reduces to:

$$\text{Da}^2 \int_{x_{\min}}^{x_{\max}} \int_0^x \left((x-v)^{1/3} - x^{1/3} \right) v^{-2/3} dv dx. \quad (4.7)$$

In writing (4.7), we have omitted the $O(1)$ factor of

$$\frac{1}{3^{1/3}\Gamma(2/3)(x_{\max} - x_{\min})} \frac{\partial {}^1B}{\partial t}(t),$$

and higher-order terms which do not contribute to the leading-order error. We wish to compute the error incurred by approximating the above double integral with the trapezoidal rule. To this end, we treat the inner integral as a function of x , and define

$$f(x) = \int_0^x \left((x-v)^{1/3} - x^{1/3} \right) v^{-2/3} dv. \quad (4.8)$$

We will make use of the closed form of f , given by

$$f(x) = \frac{x^{2/3}}{2} \left(\frac{2^{1/3} \sqrt{\pi} \Gamma(\frac{1}{3})}{\Gamma(\frac{5}{6})} - 6 \right). \quad (4.9)$$

Towards applying the trapezoidal rule to (4.7), we note $\mathcal{T}(f, [0, x_i])$ converges at a rate of $O(\Delta x^{4/3})$. This is seen by first rewriting (4.8) as

$$\int_0^{\Delta x} [(x-v)^{1/3} - x^{1/3}] v^{-2/3} dv + \int_{\Delta x}^{x_i} [(x-v)^{1/3} - x^{1/3}] v^{-2/3} dv.$$

The term on the right converges at a rate of $O(\Delta x^2)$, and the term on the left converges at a rate of $O(\Delta x^{4/3})$, which follows from expanding $(x-v)^{1/3}$ about $v=0$, and using the definition of the trapezoidal rule.

Applying the trapezoidal rule to (4.7) then gives

$$\begin{aligned} & \text{Da}^2 \int_{x_{\min}}^{x_{\max}} \int_0^x \left((x-v)^{1/3} - x^{1/3} \right) v^{-2/3} dv dx \\ &= \frac{\text{Da}^2 \Delta x}{2} \mathcal{T}(f(x), [0, x_m]) + \sum_{i=m+1}^{M-1} \text{Da}^2 \Delta x \mathcal{T}(f(x), [0, x_i]) \\ &+ \frac{\text{Da}^2 \Delta x}{2} \mathcal{T}(f(x), [0, x_M]) + O(\text{Da}^2 \Delta x^2), \end{aligned}$$

where we have let $x_{\min} = x_m = m\Delta x$, and $x_{\max} = x_M = M\Delta x$. Since $\mathcal{T}(f, [0, x_i])$ converges at a rate of $O(\Delta x^{4/3})$, the right hand side of the above is

$$\begin{aligned} & \left(\frac{\text{Da}^2 \Delta x}{2} f(x_m) + O(\text{Da}^2 \Delta x^{7/3}) \right) + \sum_{i=m+1}^{M-1} (\text{Da}^2 \Delta x f(x_i) + O(\text{Da}^2 \Delta x^{7/3})) \\ &+ \left(\frac{\text{Da}^2 \Delta x}{2} f(x_M) + O(\text{Da}^2 \Delta x^{7/3}) \right) + O(\text{Da}^2 \Delta x^2). \end{aligned}$$

To compute our results in Section (5), we took $x_{\min} = 0.2$, $x_{\max} = 0.8$, in accordance with the literature (Edwards and Jackson, 2002). Hence, in the above sum there are approximately $0.6N = 0.6\Delta x^{-1}$ terms on the order of $\text{Da}^2 \Delta x^{7/3}$, and the above sum reduces to

$$\begin{aligned} & \text{Da}^2 \left(\frac{\Delta x}{2} f(x_m) + \sum_{i=m+1}^{M-1} \Delta x f(x_i) + \frac{\Delta x}{2} f(x_M) \right) + O(\text{Da}^2 \Delta x^{4/3}) \\ &+ O(\text{Da}^2 \Delta x^{5/3}). \end{aligned} \quad (4.10)$$

The largest error in (4.10) is $O(\text{Da}^2 \Delta x^{4/3})$, thus the spatial discretization error associated with (4.6d) is $O(\text{Da}^2 \Delta x^{4/3})$. When measuring convergence we used values of $x_{\min} = .25$, $x_{\max} = .75$ to facilitate progressive grid refinement; however, it is clear that these values of x_{\min} and x_{\max} do not change our argument. A similar argument shows the spatial discretization error associated with the nonlinear term (4.6e) is $O(\text{Da}^2 \Delta x^{4/3})$.

We have depicted our spatial convergence measurements for \bar{B}_1 in Figure 4.1 and tabulated them in Table 4.1. To obtain these results, we first computed a reference solution, with $\Delta x = \Delta t = 1/512$. We then created a series of test solutions with mesh width $\Delta x = 1/2^j$, for $j = 2, \dots, 7$, keeping $\Delta t = 1/512$ constant. Next, we computed \bar{B} by averaging our reference solution and test solutions at each time step with the trapezoidal rule. We computed the error between each test solution and the reference solution by taking the maximum difference of the two at each time step.

From our results, we see that our method converges at a rate of $O(\Delta x^2)$ when $\text{Da} \ll 1$, a rate of $O(\Delta x^{4/3})$ when $\text{Da} = O(1)$, and a rate of $O(\Delta x^{3/2})$ when $\text{Da} \gg 1$. The reduction in convergence when Da increases from small to moderate may be attributed to the $O(\text{Da}^2 \Delta x^{4/3})$ contributions from (4.6d) and (4.6e). There are two competing sizes of error in (4.6a)–(4.6e): one of $O(\text{Da} \Delta x^2)$ (from terms (4.6a)–(4.6c)), and one of $O(\text{Da}^2 \Delta x^{4/3})$ (from terms (4.6d)–(4.6e)). When $\text{Da}^2 \Delta x^{4/3} < \text{Da} \Delta x^2$, or $\text{Da} < \Delta x^{2/3}$, the former is larger. Conversely, when $\Delta x^{2/3} < \text{Da}$ the latter is larger.

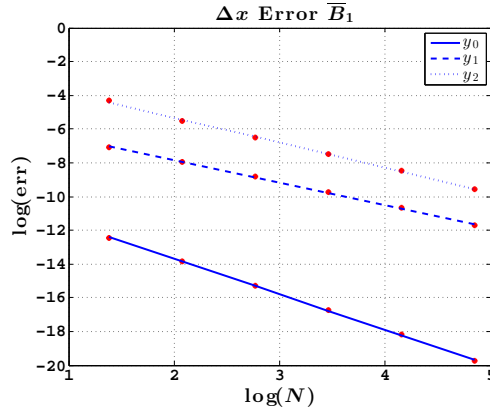


Fig. 4.1: Spatial convergence for \bar{B}_1 , $\text{Da} = .01, 1, 10$. The (solid) line $y_0 = -2.10x - 9.49$ was fit to the error when $\text{Da} = .01$. The (dashed) line $y_1 = -1.33x - 5.17$ was fit to the error when $\text{Da} = 1$. The (dotted) line $y_2 = -1.48x - 2.36$ was fit to the error when $\text{Da} = 10$. All three lines have an R^2 coefficient of $R^2 = .99$. Rate constants were taken equal to: ${}_1K_d = 1$, ${}_2K_a = 1$, ${}_2K_d = 1$, ${}_1K_a = 1/2$, ${}_1K_d = 2$, ${}_2K_a = 2$, and ${}_2K_d = 1/2$.

When $Da \gg 1$, the bound state evolves on a longer $t_w = t/Da$ time scale (Edwards, 1999); in this case the relevant equation is given by:

$$\begin{aligned} Da^{-1} \frac{d\bar{B}}{dt_w} = & (1-B) \left(1 - \frac{1}{3^{1/3}\Gamma(2/3)} \int_0^x \left(\frac{\partial B}{\partial t_w}(x-v, t_w) - \frac{\partial B}{\partial t_w}(x, t_w) \right) \frac{dv}{v^{2/3}} \right) \\ & + \frac{(1-B)}{3^{1/3}\Gamma(2/3)} \cdot \left(3x^{1/3} \frac{\partial B}{\partial t_w}(x, t_w) \right) - K\bar{B}, \\ \bar{B}(0) = & 0. \end{aligned}$$

Even a leading-order approximation to the above equation, found by taking the left hand side of the above equation equal to zero, is nonlinear and unwieldy. Nonetheless, our measurements in Figure 4.1 and Table 4.1 demonstrate that convergence is not an issue when $Da \gg 1$.

Temporal convergence was measured in an analogous manner to spatial convergence, and our results are depicted for \bar{B}_1 in Figure 4.2, which demonstrates that our method is converging at the expected rate of $O(\Delta t^2)$. Measuring temporal convergence when $Da = O(1)$ is computationally prohibitive, since spatial convergence is $O(Da^2 \Delta x^{4/3})$ in this case. Figure 4.2 indicates that temporal convergence is not a concern.

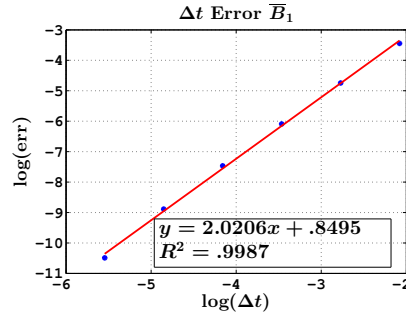


Fig. 4.2: Temporal convergence: $Da = .01$; note our second-order temporal convergence agrees with the theoretical $O(\Delta t^2)$ for a second order Adams-Bashforth method.

Table 4.1: Convergence results for B_1 . Here $Da = .01, 1, 10$.

	$Da \ll 1$	$Da = O(1)$	$Da \gg 1$
\bar{B}_1	$O(\Delta x^{2.09})$	$O(\Delta x^{1.33})$	$O(\Delta x^{1.48})$
\bar{B}_{12}	$O(\Delta x^{2.04})$	$O(\Delta x^{1.42})$	$O(\Delta x^{1.53})$
\bar{B}_2	$O(\Delta x^{2.09})$	$O(\Delta x^{1.33})$	$O(\Delta x^{1.46})$

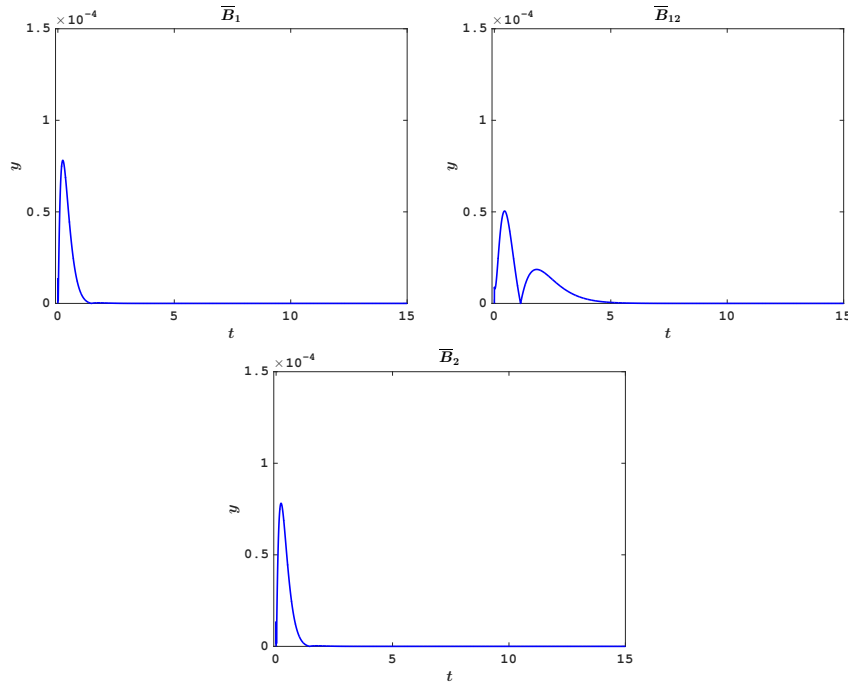


Fig. 5.1: Error in the reacting species concentrations during the injection phase, computed by taking the absolute difference between the solution of our ERC equation (3.7) and our finite-difference solution. We have taken $Da = 0.1$, and all of the rate constants equal to one.

Table 5.1: Maximum difference between our injection phase ERC approximation (3.7) and our finite difference solution, for all time. All rate constants take equal to one in both cases.

	\bar{B}_1	\bar{B}_{12}	\bar{B}_2	\mathcal{S}
$Da = .1$	7.81×10^{-5}	5.04×10^{-5}	7.81×10^{-5}	1.47×10^{-4}
$Da = .45$	1.00×10^{-3}	6.93×10^{-4}	1.00×10^{-3}	2.00×10^{-3}

5 Effective Rate Constant Approximation Verification

With our numerical method in hand, we are now in a position to verify the accuracy of our Effective Rate Constant approximations (3.7) and (3.8). We tested their accuracy of our ERC equations when $Da = 0.1$, and $Da = 0.45$; the results are below in Figures 5.1, and 5.2; and Tables 5.1, and 5.2.

From our results below, it is evident that our ERC equations serve as an accurate approximation to $\bar{\mathbf{B}}$ and the sensogram reading (2.7)—not just for small Da , but for moderate Da as well. Motivated by (Edwards and Jackson, 2002), we then ran a

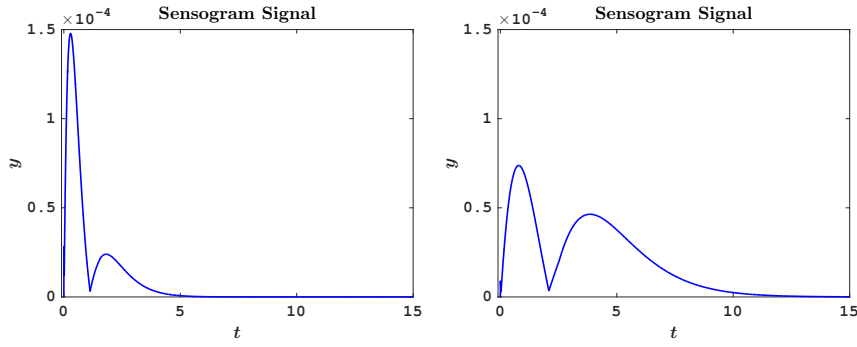


Fig. 5.2: Left: error in sensogram reading during the injection phase, calculated by taking the absolute difference between (2.7) computed with our ERC equations and (2.7) computed with our finite difference algorithm. Right: error in the sensogram (2.7) reading for the wash phase, computed in a similar manner.

Table 5.2: Maximum difference between our wash phase ERC approximation (3.8) and our finite difference solution, for all time. All rate constants take equal to one in both cases.

	\bar{B}_1	\bar{B}_{12}	\bar{B}_2	\mathcal{S}
Da = .1	3.578×10^{-5}	3.40×10^{-5}	3.58×10^{-5}	7.37×10^{-5}
Da = .45	4.33×10^{-4}	4.62×10^{-4}	4.33×10^{-4}	9.45×10^{-4}

series of simulations for different values of Da, ranging from $Da \approx 0.02$ to $Da = 150$. We measured the maximum absolute error for each value of Da, and created the logarithmic plots shown in Figure 5.3, which show that our ERC equations agree with our numerical solutions for a wide parameter range. In Figure 5.3 the error is small for $Da \ll 1$, as expected, and increases at rates which compare favorably with the $O(Da^2)$ in prediction. The error reaches an asymptote corresponding roughly to two percent absolute error. Thus, although our ERC approximations (3.7) and (3.8) are formally valid for only small values of Da, they agree with our numerical solutions for moderate and large values of Da.

6 Conclusions

Scientists are currently using optical biosensors to reveal the underlying pathway of polymerase δ during DNA translesion synthesis. Since interpreting biosensor data relies on a mathematical model, we have modeled the resulting convection-diffusion system with multiple coupled reactions on the surface. In physically relevant parameter regimes, our PDE model reduces to a set of nonlinear coupled IDEs for the reacting species concentrations. In the reaction-limited regime, this set of IDEs further simplifies to a set of nonlinear ODEs. Though this simplification is formally valid

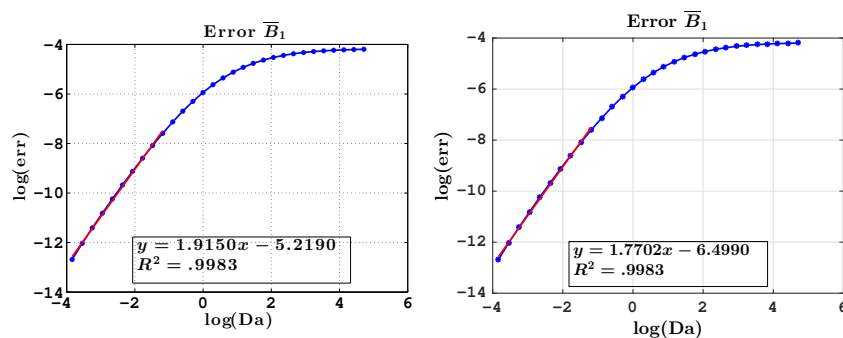


Fig. 5.3: Left: Absolute error in our injection phase approximation (3.7) over all time for different values of Da . Right: absolute error in our wash phase approximation (3.8) over all time for different values of Da . Both: the rate constants were taken equal to: ${}_1K_d = 1/2$, ${}_2K_a = 1$, ${}_2K_d = 1$, ${}_1^2K_a = 1$, ${}_1^2K_d = 2$, ${}_2^1K_a = 2$, and ${}_2^1K_d = 1/2$. Similar results hold for B_{12} , and B_2 .

only when $\text{Da} \ll 1$, the solution of our ERC equations agree with our finite-difference solution of the IDE system for a wide range of Da . Thus our ERC equations are also useful in regimes in which mass transport effects play a larger role.

Not only do our results provide chemists with a flexible tool to measure the rate constants in (1.2), we have generalized techniques previously known to be effective only for bimolecular reactions. This work also provides a basis for future study on multiple-component reactions; such areas of study include investigating other biophysical effects like cross-diffusion, and steric hindrance.

Furthermore, based on the method outlined in (Edwards and Jackson, 2002), we have developed and studied convergence of a numerical method for our nonlinear IDE system. An interesting line of future work would be to compare the present method with an extension of the method of lines algorithms described in (Zumbrum, 2013).

A Parameter Values

Below, we have tabulated parameter values from the literature.

Table A.1: Dimensional parameter ranges, taken from references (de la Torre et al., 2000), (Gen, 2013), (Rich et al., 2008), (Yarmush et al., 1996).

Parameter	Rich (2008)	Yarmush	Biacore T200	Torre
\tilde{k}_a ($10^8 \text{ cm}^3/(\text{mol} \cdot \text{s})$)	10^{-4} – 10^{-2}	$.5$ – 5×10	10^{-5} – 3×10^3	
\tilde{k}_d (10^{-3} s^{-1})	1	8.9	10^{-2} – 10^3	
\tilde{D}_1 ($10^{-7} \text{ cm}^2/\text{s}$)				4.0
\tilde{D}_2 ($10^{-7} \text{ cm}^2/\text{s}$)				6.88
\tilde{H} (1 cm)	.05	.04		
\tilde{L} (1 cm)	2			
\tilde{W} (1 cm)	1.3			
\tilde{R}_T ($10^{-12} \text{ mol}/\text{cm}^2$)	1.11×10^{-1} – 2.33×10^1	2.5–4		
\tilde{Q} (1 $\mu\text{L}/\text{min}$)	100–1500		1–100	
\tilde{V} (1 cm/s)	.153–2.88	.36–.6	.001–1.92	
\tilde{C}_u mol/cm ³	2.96×10^{-1} – 2×10^1			

The variables \tilde{W} , \tilde{Q} , represent the dimensional width, and flow rate; the other dimensional variables are as in Section 2. The flow rate is related to the velocity through the formula (Edwards, 2011)

$$\tilde{V} = \frac{6\tilde{Q}}{\tilde{W}\tilde{H}}.$$

In the absence of data for the rate constants associated with the polymerase switch between polymerase δ and polymerase η , we considered values from the literature in Table A.1. Using the dimensional values above, we calculated extremal bounds on the dimensionless variables.

Table A.2: Dimensionless parameters.

Parameter	Bound
ε	.02–.025
Re	1.23×10^{-4} –.361
Pe	1.78 – 5.24×10^4
Da	4.31×10^{-7} – 3.60×10^4
${}_2K_a$	2.63×10^{-12} – 3.80×10^{11}
${}_i^jK_a$	2.63×10^{-12} – 3.80×10^{11}
${}_iK_d$	8.89×10^{-9} – 6.33×10^{11}
${}_i^jK_d$	8.89×10^{-9} – 6.33×10^{11}
D_r	.5813
F_r	.008–39.28

The appropriate Reynolds number for our system is $\text{Re} = \tilde{V}\tilde{H}^2/(\tilde{W}\tilde{L})$; the other dimensionless variables are as in Section 2. We remark that one may be concerned about the upper bound on the Reynolds number, the lower bound on the Péclet number, and the upper bound on the Damköhler number. All of these extremal bounds were calculated using a flow rate of 1 $\mu\text{L}/\text{min}$ —the slowest flow rate possible on the Biacore T200 (Gen, 2013). Even with the fastest reactions, one can still design experiments to minimize

transport effects by increasing the flow rate \tilde{Q} (thus the velocity), decreasing the initial empty receptor concentration \tilde{R}_T , and decreasing the inflow concentration. In the case of the fastest reaction $\tilde{k}_a = 3 \times 10^9 \text{ cm}^3/(\text{mol} \cdot \text{s})$, we can take: $\tilde{Q} = 300 \text{ } \mu\text{L}/\text{min}$, $\tilde{V} = .576 \text{ cm/s}$, $\tilde{R}_T = 2 \times 10^{-13} \text{ mol/cm}^2$, $\tilde{C}_{2,u} = 2.96 \times 10^{-10} \text{ mol/cm}^3$, $\tilde{H} = .04 \text{ cm}$. These choices yield the dimensionless parameters $\text{Re} = .072$, $\text{Pe} = 1048.19$, $\text{Da} = 3.98$; these values are perfectly in line with our analysis, and the validity of our ERC equations.

References

- S. Austin. Haemostasis. *Medicine*, 37(3):133–136, 2009.
- C. Bertucci, A. Piccoli, and M. Pistolozzi. Optical biosensors as a tool for early determination of absorption and distribution parameters of lead candidates and drugs. *Combinatorial Chemistry and High Throughput Screening*, 10(6):433–440, 2007.
- J. G. de la Torre, M. L. Huertas, and B. Carrasco. Calculation of hydrodynamic properties of globular proteins from their atomic-level structure. *Biophysical Journal*, 78(2):719–730, 2000.
- D. A. Edwards. Estimating rate constants in a convection–diffusion system with a boundary reaction. *IMA Journal of Applied Mathematics*, 63(1):89–112, 1999.
- D. A. Edwards. Biochemical reactions on helical structures. *SIAM Journal on Applied Mathematics*, 42(4):1425–1446, 2000.
- D. A. Edwards. The effect of a receptor layer on the measurement of rate constants. *Bulletin of Mathematical Biology*, 63(2):301–327, 2001.
- D. A. Edwards. Convection effects in the biacore dextran layer: Surface reaction model. *Bulletin of Mathematical Biology*, 68:627–654, 2006.
- D. A. Edwards. Transport effects on surface reaction arrays: Biosensor applications. *Mathematical Biosciences*, 230(1):12–22, 2011.
- D. A. Edwards and S. Jackson. Testing the validity of the effective rate constant approximation for surface reaction with transport. *Applied Mathematics Letters*, 15(5):547–552, 2002.
- D. A. Edwards, B. Goldstein, and D. S. Cohen. Transport effects on surface-volume biological reactions. *Journal of Mathematical Biology*, 39(6):533–561, 1999.
- E. C. Friedberg. Suffering in silence: the tolerance of DNA damage. *Nature Reviews Molecular Cell Biology*, 6(12):943–953, 2005.
- BIACore T200 data file*. General Electric Life Sciences, GE Healthcare Bio-Sciences AB, Björkgatan 30, 751 84 Uppsala, Sweden, April 2013.
- R. Karlsson and A. Fält. Experimental design for kinetic analysis of protein-protein interactions with surface plasmon resonance biosensors. *Journal of immunological methods*, 200(1):121–133, 1997.
- K. Lebedev, S. Mafé, and P. Stroeve. Convection, diffusion, and reaction in a surface-based biosensor: Modeling of cooperativity and binding site competition and in the hydrogel. *Journal of Colloid Interface Science*, 296:527–537, 2006.
- A. R. Lehmann, A. Niimi, T. Ogi, S. Brown, S. Sabbioneda, J. F. Wing, P. L. Kannouche, and C. M. Green. Translesion synthesis: Y-family polymerases and the polymerase switch. *DNA repair*, 6(7):891–899, 2007.
- T. A. Morton, D. G. Myszka, and I. M. Chaiken. Interpreting complex binding kinetics from optical biosensors: a comparison of analysis by linearization, the integrated rate equation, and numerical integration. *Analytical biochemistry*, 227(1):176–185, 1995.
- Q. Nie, Y-T. Zhang, and R. Zhao. Efficient semi-implicit schemes for stiff systems. *Journal of Computational Physics*, 214(2):521–537, 2006.
- B. S. Plosky and R. Woodgate. Switching from high-fidelity replicases to low-fidelity lesion-bypass polymerases. *Current opinion in genetics & development*, 14(2):113–119, 2004.
- M. Raghaven, M. Y. Chen, L. N. Gastinel, and P. J. Bjorkman. Investigation of the interaction between class I MHC-related F^c receptor and its immunoglobulin G ligand. *Immunity*, 1(4):303–315, 1994.
- R. L. Rich and D. Myszka. Survey of the 2009 commercial optical biosensor literature. *Journal of Molecular Recognition*, 24(6):892–914, 2011.
- R. L. Rich and D. G. Myszka. Extracting kinetic rate constants from binding responses. In M. A. Cooper, editor, *Label-free bioeensors*. Cambridge University Press, 2009.

- R. L. Rich, M. J. Cannon, J. Jenkins, P. Pandian, S. Sundaram, R. Magyar, J. Brockman, J. Lambert, and D. G. Myszka. Extracting kinetic rate constants from surface plasmon resonance array systems. *Analytical Biochemistry*, 373(1):112–120, 2008.
- M. L. Yarmush, D. B. Patankar, and D. M. Yarmush. An analysis of transport resistances in the operation of BIAcore; implications for kinetic studies of biospecific interactions. *Molecular Immunology*, 33(15):1203–1214, 1996.
- Z. Zhuang, R. E. Johnson, L. Haracska, L. Prakash, S. Prakash, and S. J. Benkovic. Regulation of polymerase exchange between $\text{pol}\eta$ and $\text{pol}\delta$ by monoubiquitination of pcna and the movement of dna polymerase holoenzyme. *Proceedings of the National Academy of Sciences*, 105(14):5361–5366, 2008.
- M. Zumburum. *Extensions For a Surface-Volume Reaction Model With Application To Optical Biosensors*. PhD thesis, University of Delaware, 2013.
- M. Zumburum and D. A. Edwards. Multiple surface reactions in arrays with applications to optical biosensors. *Bulletin of Mathematical Biology*, 76(7):1783–1808, 2014.
- M. Zumburum and D. A. Edwards. Conformal mapping in optical biosensor applications. *Journal of Mathematical Biology*, 71(3):533–550, 2015.